Chapter 3

Multi-Scale Effective Elastic Micromechanical Model for Bone Tissues

3.1 Introduction

In this chapter, we try to develop a static multi-scale micromechanical model of bone tissue. The estimation of the effective stiffness of bone material is based on four homogenization steps (**Figure 3-1**). The first homogenization step refers to an observation scale of several hundred nanometers, where cross-linked collagen molecules form a contiguous matrix and apatite crystals nucleate and grow within the gap regions between adjacent collagen molecules, building up the mineralized collagen fibrils. At the ultrastructural scale, mineralized collagen fibrils are present in bundles and embedded as inclusions into the extrafibrillar mineral foam which is composed of hydroxyapatite, ultrastructural water and non-collageneous proteins. The last homogenization step refers to extravascular bone material at an observation scale of 100 μm, where osteocyte lacunae are embedded in extracellular bone matrix.

3.2 Mineralized Collagen Fibrils

The structural organization of the mineralized collagen fibril proposed by Fratzl et al. [4, 9] is adopted. In this interpretation, mineral crystals are observed to be randomly distributed in the plane perpendicular to the longitudinal axis of the mineralized collagen

fibrils. In our model, an individual agglomeration of apatite crystals is approximated as a prolate spheroid whose major axe is oriented along the x_1 direction. If we assume that an individual agglomeration of apatite crystals fills the gap region during the mineralization process, the final aspect ratio of mineral crystals can be estimated reasonably from the length and the equatorial width of the gap region. The length of the gap region is taken as 40 nm following the Hodge-Petruska scheme [11] (**Figure 3-2**). While the available equatorial width of the gauge region is 1.5 nm in an unmineralized collagen fibril, x-ray diffraction studies have showed that mineral crystals grow wider than the available space, up to 3 nm, compressing the collagenous matrix in which they are embedded [4] (**Figure 3-3**). Therefore, the aspect ratio of a mineral crystal that is fully occupying the gap region is about $40/3$.

3.2.1 Phase Stiffness Values

In order to estimate the effective stiffness of the mineralized collagen fibril, $\boldsymbol{C}_{fib}$, the material properties of apatite crystals, collagen and ultrastructural water (with non-collagenous proteions) phases are required. It is almost impossible to obtain these values from the macroscopic tests of any collagenous tissue since there is a significant level of porosity which underestimates the elastic moduli. In addition, the involvement of microstructural units and interfaces in the deformation of bone tissue (such as lamellar interfaces and cement lines) also affects the measured material properties.

Keeping these constraints in mind, the elastic constants of apatite crystals are chosen from the study by Gilmore and Katz [12]. In their work, the isotropic elastic

contents of crystalline apatite solids are determined from measurements of elastic wave velocities through enamel powders under pressure. The crystallites of enamel are in the form of carbonated hydroxyapatite which is similar to crystallites of bone [13]. Therefore, the bulk modulus and shear modulus of apatite crystals are selected as $k_{HA} = 80$ GPa and $\mu_{HA} = 45$ GPa.

The elastic modulus of collagen molecule is taken as $E_{col} = 2.9$ GPa from the study by Sasaki and Odajima [14]. In their work, X-ray diffractometry was performed on bovine Achilles tendon, and the stress-strain curve of the collagen molecule was constructed by assuming a molecular packing pattern in the cross-section of the specimen and adopting geometrical calculations. The Poisson's ratio of a collagen molecule is not available in the literature; therefore, a typical value of 0.3 is assumed for the computations.

The bulk modulus and shear modulus of ultrastructural water (with non-collagenous proteins) are taken as the standard values of water, $k_{uw} = 2.3$ GPa and $\mu_{uw} = 0$ GPa. In case of dry tissues, $\boldsymbol{C}_{uw} = 0$ is adopted.

3.2.2 The Micromechanical Model

Within the framework of micromechanics, the effective stiffness tensor of the mineralized collagen fibril $\boldsymbol{C}_{fib}$ can be expressed in terms of the stiffness tensor of the collagenous matrix $\boldsymbol{C}_{col}$, the stiffness tensor of the apatite crystals $\boldsymbol{C}_{HA}$, the stiffness

tensor of ultrastructural water (with non-collagenous proteins) $\boldsymbol{C}_{uw}$, the corresponding volume fractions $\phi_{HA,fib}$ and $\phi_{uw,fib}$, and the Eshelby's tensor $\boldsymbol{S}$ (for spheroid and sphere) (cf. **Appendix I**) [15]. It reads as

$$\boldsymbol{C}_{fib} = \boldsymbol{C}_{col} \bullet \left[\boldsymbol{I} + \sum_{a=1}^{2} \phi_a \left(\boldsymbol{A}_a + \boldsymbol{S}_a \right)^{-1} \left[I - \sum_{r=1}^{2} \phi_r \boldsymbol{S}_r \left(\boldsymbol{A}_r + \boldsymbol{S}_r \right)^{-1} \right]^{-1} \right] \tag{3.1}$$

where

$$\phi_1 = \phi_{HA,fib}, \quad \boldsymbol{A}_1 = \left(\boldsymbol{C}_{HA} - \boldsymbol{C}_{col} \right)^{-1} \bullet \boldsymbol{C}_{col} \tag{3.2}$$

$$\phi_2 = \phi_{uw,fib}, \quad \boldsymbol{A}_2 = \left(\boldsymbol{C}_{uw} - \boldsymbol{C}_{col} \right)^{-1} \bullet \boldsymbol{C}_{col} \tag{3.3}$$

The model generates a transversely isotropic stiffness tensor for the mineralized collagen fibril. Elastic constants increase with increasing volume fraction of apatite crystals. However, the elastic modulus along the longer axis of the mineralized collagen fibril C_{1111} increases at a much greater rate than the other moduli (**Figure 3-4**). C_{1111} at a volume fraction of 0.6 is about 12 times greater than the modulus of the unmineralized fibril. On the other hand, the transverse elastic constant C_{2222} $(= C_{3333})$ and the two shear moduli increase only threefold by a mineral volume fraction of 0.6. These observations indicate that the reinforcement of collagenous matrix with prolate spheroid shaped apatite crystals increases the stiffness along the longer axis of the apatite crystals preferentially. The Poisson's ratio ν_{21} $(= \nu_{31})$ decreases with increasing mineral volume fraction, indicating that reinforcement with apatite crystals constrains the transverse lateral strains within $x_2 - x_3$ plane when the fibrils are stressed along the longitudinal axis. The strain

along the longitudinal axis in response to stress applied along the transverse plane (i.e., $\nu_{12} = \nu_{13}$) exhibits a small decline with increasing mineral volume fraction.

The value of an elastic constant at the aspect ratio of 40/3 is taken as the reference and the percent variation of the elastic constant with respect to this value is plotted as a function of aspect ratio at a mineral volume fraction of 0.42 (**Figure 3-5**). The aspect ratio covers a range of 5 to 25, and the greater ratio represents a more needle-like apatite crystal shape. E_1 and ν_{21} ($=\nu_{31}$) display notable variations with different aspect ratio whereas the change in the remaining elastic constants are within 5%. At a fixed mineral volume fraction, the stiffness of the mineralized collagen fibril along its longitudinal axis increases when the crystal shape becomes more needle-like.

3.3 Extrafibrillar Mineral Foam

The elastic properties of the extrafibrillar mineral foam are estimated from those of hydroxyapatite, ultrastructural water and non-collagenous proteins. The hydroxyapatite crystals in the foam are considerable disordered and establish a continuum [16-20]. Therefore, within the framework of micromechanics, the effective stiffness tensor of the extrafibrillar mineral foam $\boldsymbol{C}_{ef}$ can be expressed in terms of the stiffness tensor of the apatite crystals $\boldsymbol{C}_{HA}$, the stiffness tensor of ultrastructural water (with non-collagenous proteins) $\boldsymbol{C}_{uw}$, the volume fraction of the inclusion ϕ_{uw}, and the Eshelby's tensor $\boldsymbol{S}$ (for sphere) (cf. **Appendix I**) [21].

The same as the model of mineralized collagen fibril, the bulk modulus and shear modulus of ultrastructural water (with non-collagenous proteins) are taken as the standard values of water, $k_{uw} = 2.3$ GPa and $\mu_{uw} = 0$ GPa . In case of dry tissues, $\boldsymbol{C}_{uw} = 0$ is adopted. Accordingly,

$$\boldsymbol{C}_{ef} = \boldsymbol{C}_{HA} \bullet \left[\boldsymbol{I} + \phi_{uw} \left(\boldsymbol{A} + \left(1 - \phi_{uw}\right) \boldsymbol{S} \right)^{-1} \right] \tag{3.4}$$

where

$$\boldsymbol{A} = \left(\boldsymbol{C}_{uw} - \boldsymbol{C}_{HA} \right)^{-1} \bullet \boldsymbol{C}_{HA} \tag{3.5}$$

The stiffness tensor $\boldsymbol{C}_{ef}$ is isotropic, which is consistent with the study by Lees et al. [22].

3.4 Extracellular Bone Material or Ultrastructure

Within a RVE of bone ultrastructure with characteristic length 3-10 μm, spheroidal fibrillar inclusions are embedded in a contiguous matrix built up by the mineral foam material with different orientations. Using a Ju-Chen first order micromechanical approximation [15, 21] and performing the orientational averaging procedures (cf. **Appendix III**) [23], the effective stiffness tensor of ultrastructure $\boldsymbol{C}_{ultra}$ can be expressed in terms of the stiffness tensor of the mineralized collagen fibrils $\boldsymbol{C}_{fib}$, the stiffness tensor of the extrafibrillar mineral foam $\boldsymbol{C}_{ef}$, the volume fraction of the inclusion (mineralized collagen fibrils) ϕ_{fib}, and the Eshelby's tensor $\boldsymbol{S}$ (for spheroid) (cf. **Appendix I**) [15]. Therefore, we have

$$\boldsymbol{C}_{ultra} = \boldsymbol{C}_{ef} \bullet \left(\boldsymbol{I} + \phi_{fib} \boldsymbol{\Omega} \bullet \boldsymbol{\Lambda}^{-1} \right) \tag{3.6}$$

where the fourth-rank tensor $\boldsymbol{\Lambda}$ and $\boldsymbol{\Omega}$ can be derived from Eqs. (3.39) and (3.40) with the fibril orientation pattern, and

$$\boldsymbol{A} = \left(\boldsymbol{C}_{fib} - \boldsymbol{C}_{ef}\right)^{-1} \bullet \boldsymbol{C}_{ef} \tag{3.7}$$

3.5 Extravascular Bone Material

Within a RVE of extravascular bone material with characteristic length 100 μm, spheroid voids (osteocyte lacunae) (**Figure 3-6**) which are typically 2 μm in diameter and 6 μm in long axis [24] are embedded in a contiguous matrix built up by the extracellular bone material obtained from the previous homogenization step. Adopting a Ju-Chen first order micromechanical approximation [15, 21], the effective stiffness tensor of extravascular bone material $\boldsymbol{C}_{ex}$ can be expressed in terms of the stiffness tensor of the lacunae $\boldsymbol{C}_{lac}$ which is assumed 0 here, the stiffness tensor of the ultrastructure $\boldsymbol{C}_{ultra}$, the volume fraction of the void ϕ_{lac}, and the Eshelby's tensor $\boldsymbol{S}$ (for spheroid) (cf. **Appendix II**) [15]; resulting in

$$\boldsymbol{C}_{ex} = \boldsymbol{C}_{ultra} \bullet \left[\boldsymbol{I} + \phi_{lac}\left(\boldsymbol{A} + \left(1 - \phi_{lac}\right)\boldsymbol{S}\right)^{-1}\right] \tag{3.8}$$

where

$$\boldsymbol{A} = \left(\boldsymbol{C}_{lac} - \boldsymbol{C}_{ultra}\right)^{-1} \bullet \boldsymbol{C}_{ultra} \tag{3.9}$$

3.6 Results and Discussions

One important assumption of the model of mineralized collagen fibrils is that collagen molecules establish a continuum in which apatite crystals are embedded. This assumption requires the knowledge of how individual collagen molecules are linked and how the intermolecular space is occupied. There is an abundance of covalent crosslinks, enzymatic as well as nonenzymatic, which links the collagen network [25, 26]. The continuum of the collagen molecules is further facilitated by the mineralization process which reduces the lateral spacing between collagen molecules and brings them closer [27, 28]. In addition, the intermolecular spaces are filled with water molecules which are bound to collagen molecules via permanent dipole bonds [29]. Therefore, these bound water molecules could be considered as the extensions of collagen molecules to the intermolecular spaces. In our model, the contributions of some intermolecular voids are considered as an extra ultrastructural water (with non-collagenous proteins) phase, resulting in the more accurate effective stiffness.

It is not a simple issue to predict the volume fraction of apatite crystals in mineralized collagen fibrils. The difficulty arises from obtaining samples at the fibrillar level, and, unlike weight fraction, there is no straightforward way to measure volume fraction experimentally. Therefore, the model depends on the predictions of earlier studies for the volume fraction of apatite crystals [9, 27, 30]. These predictions are based on the fact that the lateral spacing of collagen molecules reduces when apatite crystals replace water molecules during the course of mineralization. Using this lateral reduction in lateral spacing of mineralized fibers, the upper limit for the mineral volume fraction of

collagen fibrils is estimated at 0.48, the lower limit is at 0.15, and the mineral volume fraction of fully mineralized bone is predicted as 0.42 [9].

There is no published experimental data on the modulus of individual mineralized collagen fibrils due to their small size. Existing data are obtained either from mechanical tests of macroscopic specimens or from nanoindentation test. It would be more appropriate to compare our prediction with the experimental data from nanoindentation test [2, 7, 10] . The prediction of the model is in agreement with the experimental data (**Figure 3-7**). The model predicts that the lateral shrinkage of collagen fibrils when stressed longitudinally decreased with increasing mineral content. The Poisson's ratio ν_{21} $(=\nu_{31})$ at a fully mineralized range converges to 0.05 (**Figure 3-4**). This reduction in lateral deformation may have important implications from the structural stability point of view. Limited lateral shrinkage under longitudinal stress would constrain the mobility of the mineralized collagen fibril and improve the fibril's attachment to its environment under tension. This limited mobility may in turn render additional stiffness to bone tissue.

The experimental validation of the homogenization scheme for the extrafibrillar mineral foam requires determination of the ultrastructural water volume fraction ϕ_{uw} from tissue experiments. Since $\phi_{uw} = 1 - \phi_{HA}$ and ϕ_{HA} can be determined from weighting experiments of wet, dried, and dried demineralized tissues, through the following equation [27]

$$\phi_{HA} = WF_{HA} \times \frac{\rho_w}{\rho_{HA}} \tag{3.10}$$

where WF_{HA} is the weight fraction of hydroxyapatite in the wet tissue, ρ_w is the mass density of the wet tissue, and $\rho_{HA} = 3.00$ g/cm^3 [27] is the mass density of hydroxyapatite (**Table 3-1**). The comparison of elastic constant C_{1111} and the Poisson ratio are shown in **Figure 3-8**.

Table 3-1. Composition and stiffness of the extrafibrillar mineral foam

Tissue	$\rho_w \left(\text{g/cm}^3\right)$	WF_{HA}	ϕ_{HA} Eq.(3.10)	$C_{1111}^{\text{exp}} \left(\text{GPa}\right)$
enamel	2.90[a]	0.96[b]	0.9280	125.0[a]
enamel	2.90[a]	0.96[b]	0.9280	115.0[a]

[a] Lees et al. [3] [b] Cuy et al. [8]

In order to demonstrate the validity of the present model at the ultrastructural scale and extravascular level, the experimental data are obtained from the study by Hellmich et al. [1] and reorganized in **Table 3-2** and **Table 3-3** (cf **Appendix IV**). The volume fraction of the osteocyte lacunae ϕ_{lac} is selected as 0.025 based on the confocol images [5]. The comparisons between the model and the data are then shown in **Figure 3-9** and **Figure 3-10**. Generally, our numerical results are close to the experimental data.

Table 3-2. Experimental data [1]

Tissue	State	$C_{1111}^{\exp}$ (GPa)	ϕ_{fib}	ϕ_{HA}	ϕ_{uw}
cow tibia	wet	31.65	0.50	0.27	0.36
cow tibia	wet	31.50	0.50	0.27	0.37
cow tibia	wet	29.32	0.54	0.26	0.40
cow tibia	wet	30.10	0.52	0.26	0.40
cow tibia	wet	30.42	0.51	0.26	0.40
cow tibia	wet	30.86	0.52	0.27	0.37
cow tibia	wet	31.61	0.49	0.28	0.35
cow tibia	wet	31.96	0.51	0.27	0.35
cow tibia	wet	35.99	0.50	0.27	0.36
deer antler	wet	16.51	0.62	0.20	0.55
deer antler	wet	17.17	0.64	0.21	0.54
cow tibia	dry	41.96	0.60	0.31	0.20
deer antler	dry	24.22	0.74	0.23	0.36
deer antler	dry	28.26	0.77	0.25	0.30

Table 3-3. Experimental data [1]

Tissue	State	$C_{3333}^{\exp}$ (GPa)	ϕ_{fib}	ϕ_{HA}	ϕ_{uw}
cow tibia	wet	20.40	0.49	0.27	0.36
cow tibia	wet	20.10	0.49	0.26	0.39
cow tibia	wet	19.70	0.50	0.25	0.41
cow tibia	wet	20.10	0.49	0.26	0.39
cow tibia	wet	21.80	0.54	0.27	0.37
cow tibia	wet	21.80	0.48	0.27	0.37
cow tibia	wet	22.80	0.51	0.27	0.37
deer antler	wet	10.10	0.64	0.21	0.54
deer antler	wet	10.00	0.64	0.21	0.53
cow tibia	dry	25.50	0.60	0.32	0.18
deer antler	dry	13.90	0.75	0.25	0.31
deer antler	dry	15.40	0.76	0.27	0.25
rabbit femur					
BAPN	wet	22.70	0.45	0.26	0.39
BAPN	wet	21.80	0.47	0.26	0.38
BAPN	wet	21.70	0.47	0.26	0.38
BAPN	wet	21.50	0.47	0.26	0.40
BAPN	wet	19.20	0.48	0.25	0.42
BAPN	wet	18.00	0.46	0.24	0.45
fluor	wet	20.50	0.39	0.26	0.40
fluor	wet	21.20	0.38	0.27	0.39
fluor	wet	14.00	0.37	0.23	0.50
fluor	wet	10.90	0.32	0.17	0.63

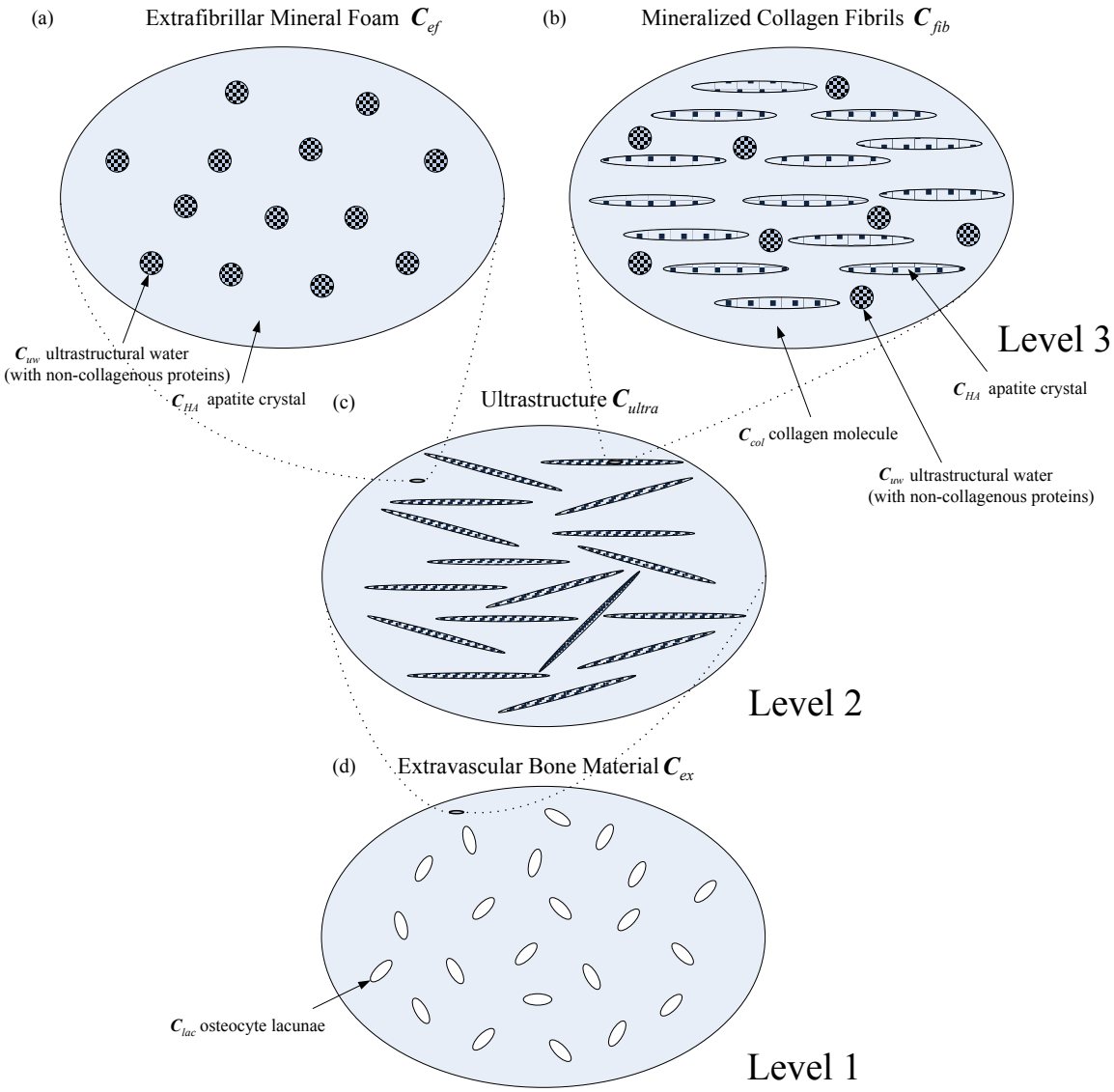

Figure 3-1. Micromechanical representation of bone tissue based on four homogenization steps: (a) Extrafibrillar mineral foam. (b) Mineralized collagen fibrils. (c) Ultrastructure. (d) Extravascular bone material.

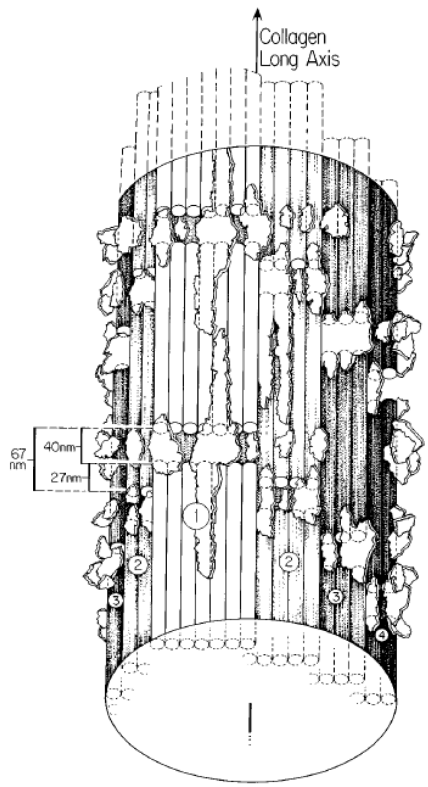

Figure 3-2. Schematic diagram of early surface and gap region mineralization in a collagen fibril [6].

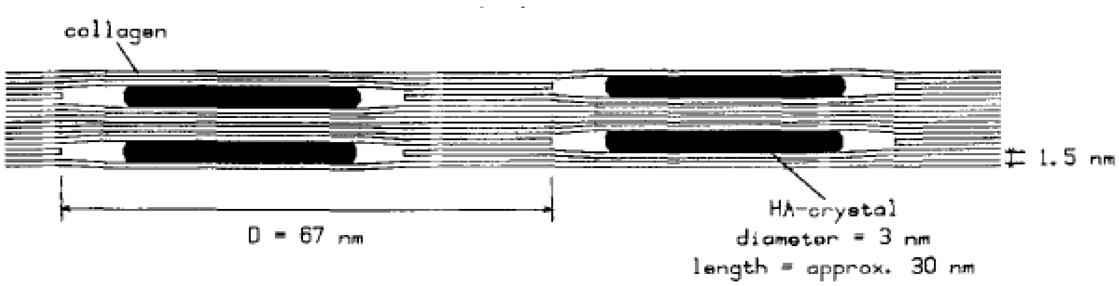

Figure 3-3. Model for the calcification process: Mineral crystals increase in thickness until they reach the maximum thickness of 3 nm [4].

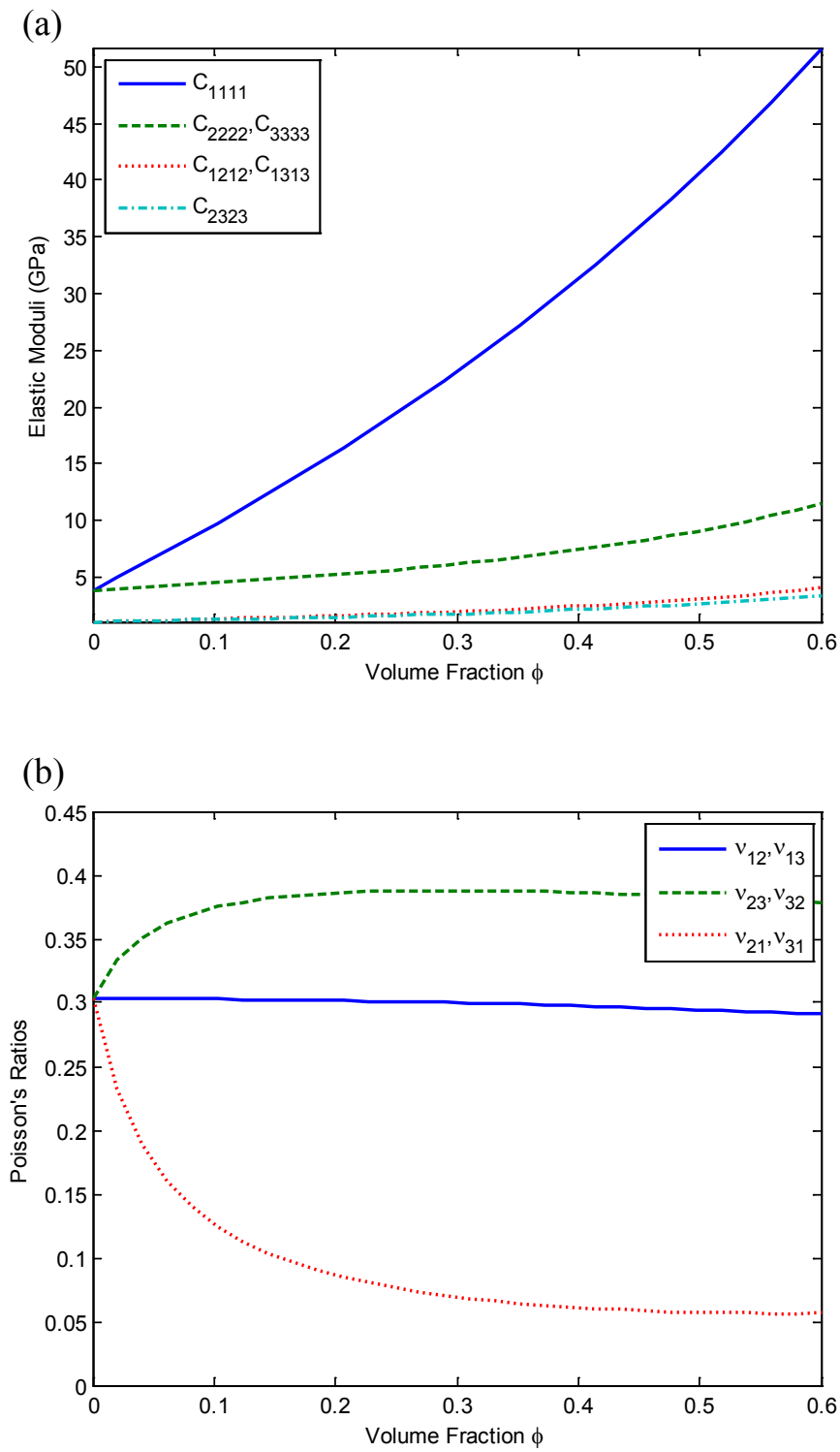

Figure 3-4. Change in the (a) elastic moduli and (b) Poisson's ratios of mineralized collagen fibrils with increasing volume fraction of apatite crystals.

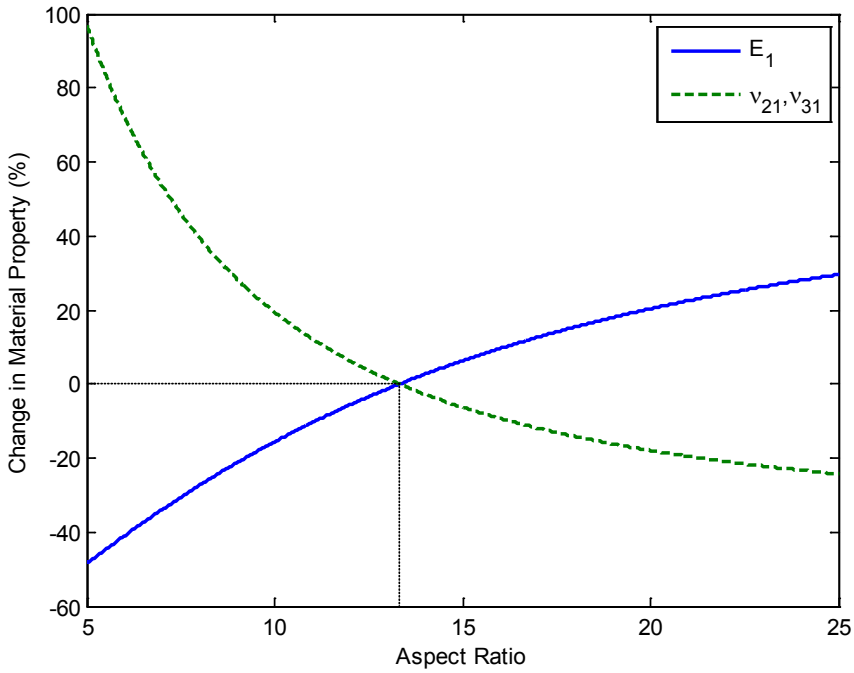

Figure 3-5. Percent change in the elastic constants of mineralized collagen fibrils with increasing aspect ratio of apatite crystals at a volume fraction of 0.42. The percent change is calculated with respect to the elastic constants at the aspect ratio of 40/3.

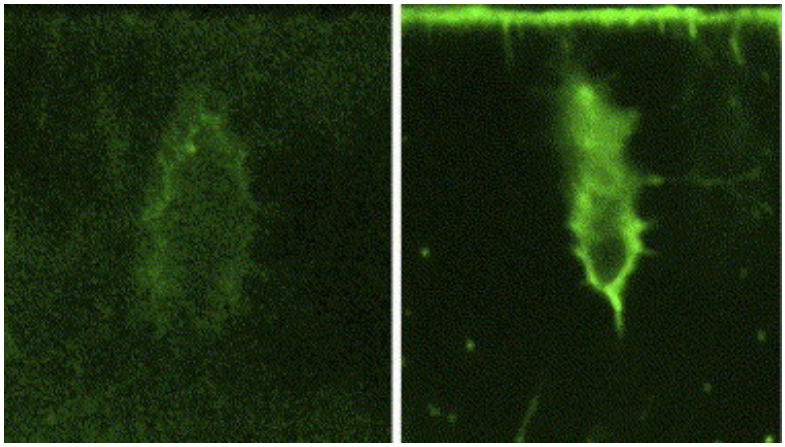

Figure 3-6. Confocol images of osteocyte lacunae and canaliculae exiting lacunae for extinct lamellar specimen. [5]

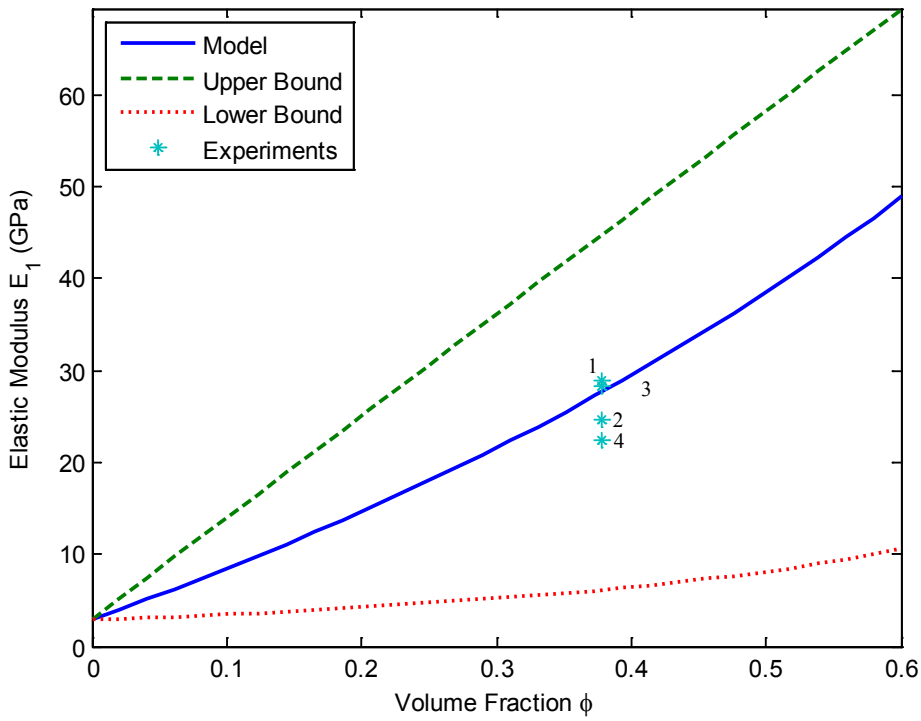

Figure 3-7. The comparison of the predicted elastic modulus E_1 (along the longitudinal axis) of the mineralized collagen fibrils and those experimentally measured via nanoindentation.

1. human tibial cortical bone, 28.9 GPa ± 1.8 GPa [2]
2. human tibial cortical bone osteons, 24.6 GPa ± 1.3 GPa [7]
3. human tibial cortical bone interstitial lamellae, 28.2 GPa ± 1.1 GPa [7]
4. tracular bone, 22.5 ± 3.1 GPa [10].

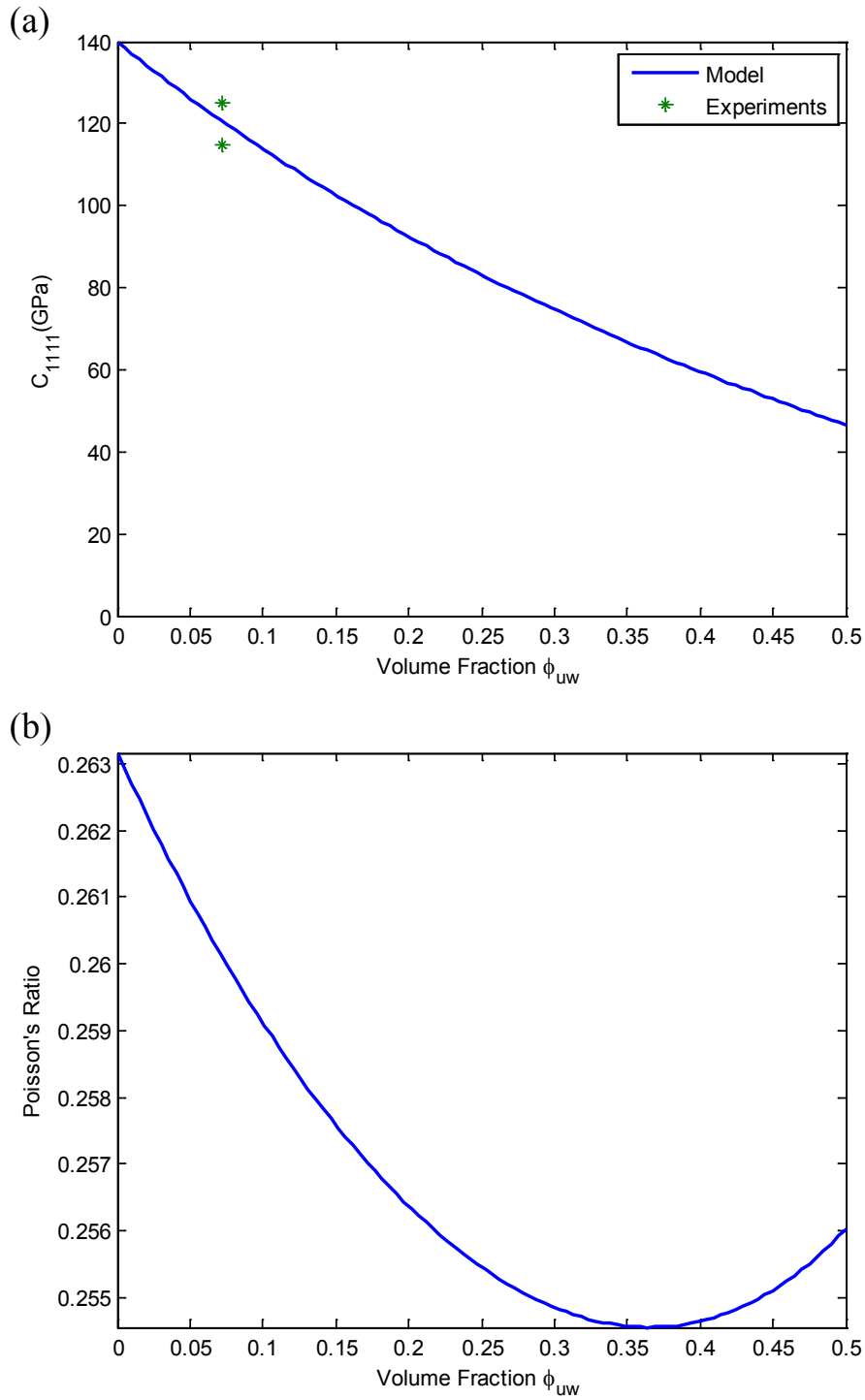

Figure 3-8. (a) Axial stiffness C_{1111} and (b) Poisson's ratio of the extrafibrillar mineral foam as a function of ultrastructural water volume fraction ϕ_{uw}.

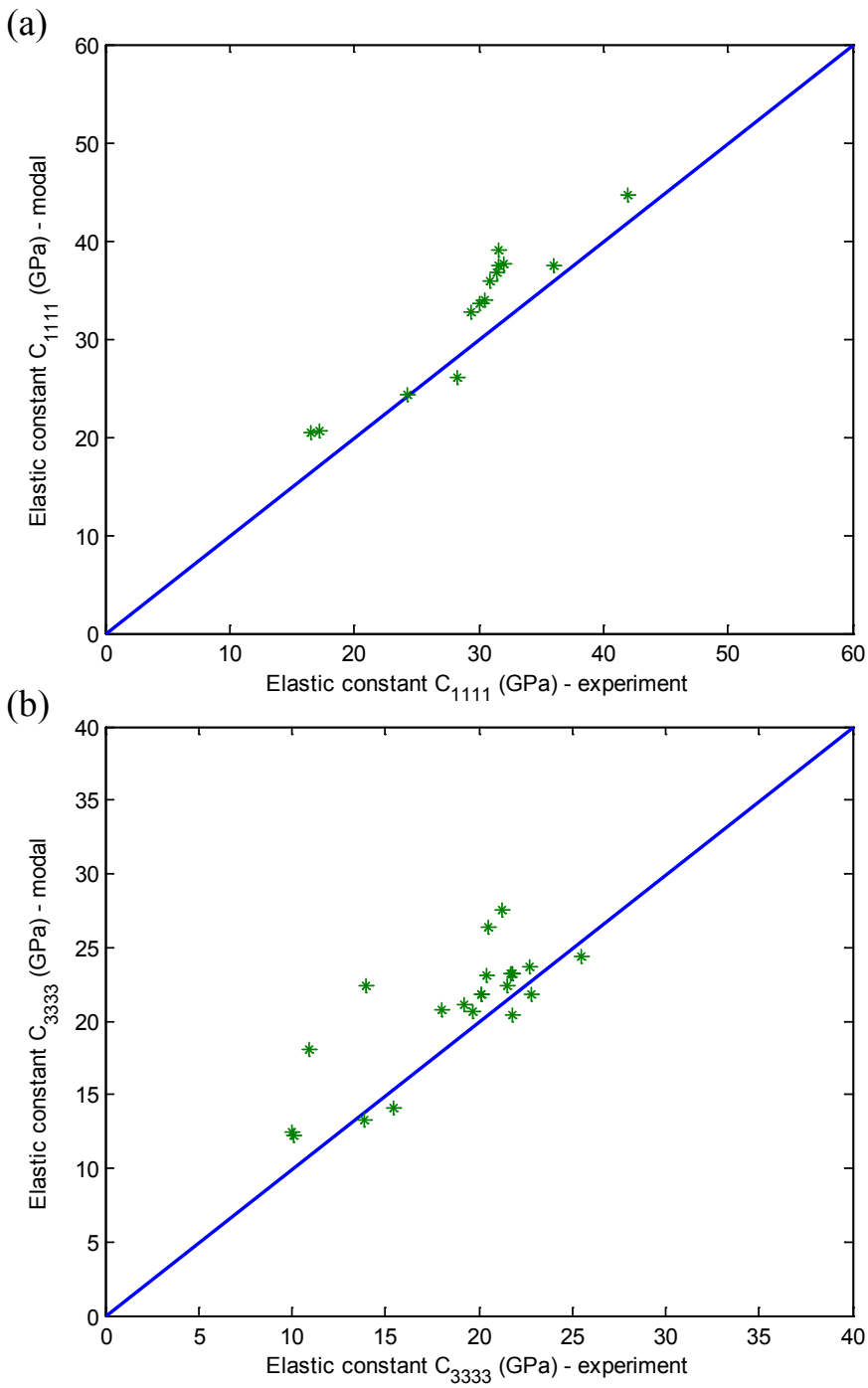

Figure 3-9. Comparison between stiffness predictions of micromechanical model and experimental stiffness values (at ultrastructural scale): (a) axial stiffness C_{1111} (b) radial stiffness C_{3333}, see also **Table 3-2** and **Table 3-3**.

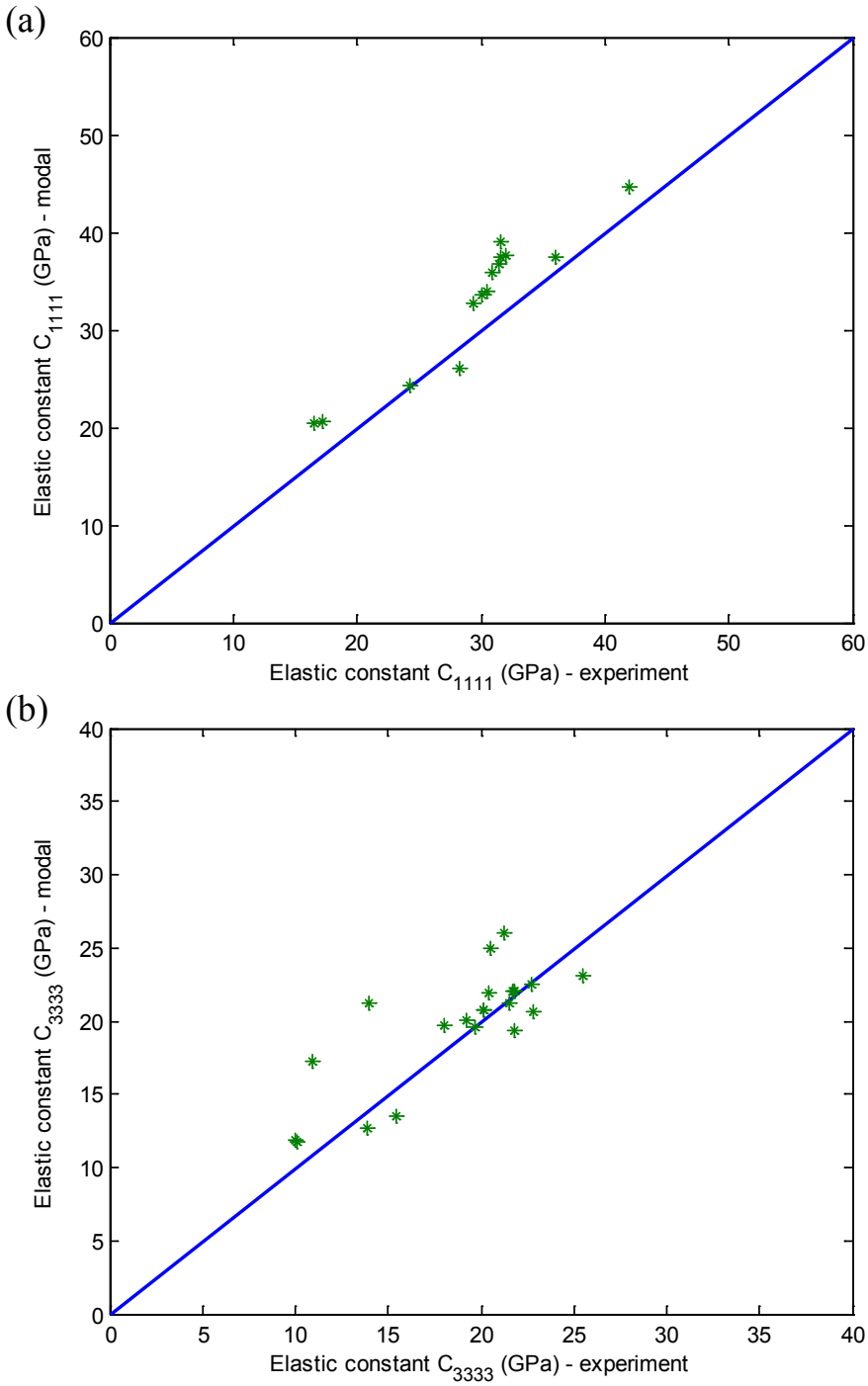

Figure 3-10. Comparison between stiffness predictions of micromechanical model and experimental stiffness values (at extravascular level): (a) axial stiffness C_{1111} (b) radial stiffness C_{3333}, see also **Table 3-2** and **Table 3-3**.

3.7 Appendix I: The Interior-Point Eshelby's Tensor

For a spheroidal inclusion aligned with the x_1-axis, the components of (interior point) Eshelby's tensor can be explicitly described as

$$S_{ijkl} = \frac{1}{4\left(1-\nu_0\right)}\left[S_{IK}^{(1)}\left(0\right)\delta_{ij}\delta_{kl} + S_{IJ}^{(2)}\left(0\right)\left(\delta_{ik}\delta_{jl} + \delta_{il}\delta_{jk}\right)\right] \tag{3.11}$$

where

$$S_{11}^{(1)}\left(0\right) = \left[4\nu_0 + \frac{2}{\alpha^2-1}\right]g\left(0\right) + 4\nu_0 + \frac{4}{3\left(\alpha^2-1\right)} \tag{3.12}$$

$$S_{12}^{(1)}\left(0\right) = S_{13}^{(1)}\left(0\right) = \left[4\nu_0 - \frac{2\alpha^2+1}{\alpha^2-1}\right]g\left(0\right) + 4\nu_0 - \frac{2\alpha^2}{\alpha^2-1} \tag{3.13}$$

$$S_{21}^{(1)}\left(0\right) = S_{31}^{(1)}\left(0\right) = \left[-2\nu_0 - \frac{2\alpha^2+1}{\alpha^2-1}\right]g\left(0\right) - \frac{2\alpha^2}{\alpha^2-1} \tag{3.14}$$

$$S_{22}^{(1)}\left(0\right) = S_{23}^{(1)}\left(0\right) = S_{32}^{(1)}\left(0\right) = S_{33}^{(1)} = \left[-2\nu_0 + \frac{4\alpha^2-1}{4\left(\alpha^2-1\right)}\right]g\left(0\right) + \frac{\alpha^2}{2\left(\alpha^2-1\right)} \tag{3.15}$$

$$S_{11}^{(2)}\left(0\right) = \left[-4\nu_0 + \frac{4\alpha^2-2}{\alpha^2-1}\right]g\left(0\right) - 4\nu_0 + \frac{12\alpha^2-8}{3\left(\alpha^2-1\right)} \tag{3.16}$$

$$S_{12}^{(2)}\left(0\right) = S_{13}^{(2)}\left(0\right) = S_{21}^{(2)}\left(0\right) = S_{31}^{(2)} = \left[-\nu_0 - \frac{\alpha^2+2}{\alpha^2-1}\right]g\left(0\right) - 2\nu_0 - \frac{2}{\alpha^2-1} \tag{3.17}$$

$$S_{22}^{(2)}\left(0\right) = S_{23}^{(2)}\left(0\right) = S_{32}^{(2)}\left(0\right) = S_{33}^{(2)} = \left[2\nu_0 - \frac{4\alpha^2-7}{4\left(\alpha^2-1\right)}\right]g\left(0\right) + \frac{\alpha^2}{2\left(\alpha^2-1\right)} \tag{3.18}$$

where $g\left(0\right)$ is given by

$$g(0)=\begin{cases}\dfrac{\alpha}{\left(\alpha^2-1\right)^{3/2}}\left[\cosh^{-1}\alpha-\alpha\left(\alpha^2-1\right)^{1/2}\right] & \text{for } \alpha>1\\ \dfrac{\alpha}{\left(1-\alpha^2\right)^{3/2}}\left[\alpha\left(1-\alpha^2\right)^{1/2}-\cos^{-1}\alpha\right] & \text{for } \alpha<1\end{cases} \tag{3.19}$$

For the special case of a spherical inclusion, the (interior point) Eshelby's tensor reduces to

$$S_{ijkl}=\frac{5\nu_0-1}{15\left(1-\nu_0\right)}\delta_{ij}\delta_{kl}+\frac{4-5\nu_0}{15\left(1-\nu_0\right)}\left(\delta_{ik}\delta_{jl}+\delta_{il}\delta_{jk}\right) \tag{3.20}$$

3.8 Appendix II: The Interior-Point Eshelby's Tensor for Inclusions in a Transversely Isotropic Matrix

For a spheroidal inclusion in a transversely isotropic matrix with stiffness tensor $\boldsymbol{C}_0$, the Eshelby's tensor $\boldsymbol{S}$ can be obtained from the fourth-order $\boldsymbol{P}$ tensor which characterizes the interaction between the inclusion and the matrix.

$$P_{ijkl} = -\left(\frac{\partial^2 \int_\Omega G_{ik}\left(\boldsymbol{x}-\boldsymbol{x}'\right) dV'}{\partial x_j \partial x_l} \right)_{(ij)(kl)} \tag{3.21}$$

In Eq. (3.21), $(ij)(kl)$ represents symmetry with respect to (ij) and (kl). $G_{ik}\left(\boldsymbol{x}-\boldsymbol{x}'\right)$ is the Green's function which gives the displacement at point $\boldsymbol{x}$ resulting from a unit force at point $\boldsymbol{x}'$.

If the long axis of the spheroidal inclusion is perpendicular to the plane of isotropy of the matrix and the aspect ratio of the inclusion is defined as

$$\alpha = \frac{a_1}{a},\ a_1 > a \tag{3.22}$$

where a_1 and a are the semi-axes of the spheroids. The non-zero components of the symmetric $\boldsymbol{P}$ tensor can be expressed in terms of two elementary integrals shown in Eq. (3.28) and Eq. (3.29) as followed [31]

$$P_{1111} = \frac{3}{16} I_1\left(C^0_{2323}, C^0_{3333} - 2C^0_{2323}, C^0_{2323} - C^0_{3333}\right) + \frac{1}{16} I_2\left(1,-1\right) \tag{3.23}$$

$$P_{1122} = \frac{1}{16} I_1\left(C^0_{2323}, C^0_{3333} - 2C^0_{2323}, C^0_{2323} - C^0_{3333}\right) - \frac{1}{16} I_2\left(1,-1\right) \tag{3.24}$$

$$P_{1133} = \frac{1}{4} I_1 \left(0, -C^0_{1133} - C^0_{2323}, C^0_{1133} + C^0_{2323}\right) \tag{3.25}$$

$$P_{3333} = \frac{1}{2} I_1 \left(0, C^0_{1111}, C^0_{2323} - C^0_{1111}\right) \tag{3.26}$$

$$P_{1313} = \frac{1}{16} I_1 \left(C^0_{1111}, -2\left(C^0_{1111} + C^0_{1133}\right), C^0_{1111} + C^0_{3333} + 2C^0_{1133}\right) - \frac{1}{16} I_2 \left(0, -1\right) \tag{3.27}$$

The elementary integral I_1 and I_2 are

$$I_1\left(l,m,n\right) = \frac{1}{C^0_{3333}C^0_{2323}} \int_{-1}^{1} \frac{\alpha}{\left[1-\left(1-\alpha^2\right)\xi^2\right]^{3/2}} \frac{\left(1+m\xi^2+n\xi^4\right)}{\left[\gamma_1^2+\left(1-\gamma_1^2\right)\xi^2\right]\left[\gamma_2^2+\left(1-\gamma_2^2\right)\xi^2\right]} d\xi \tag{3.28}$$

$$I_2\left(l,m\right) = \int_{-1}^{1} \frac{\alpha}{\left[1-\left(1-\alpha^2\right)\xi^2\right]^{3/2}} \frac{\left(1+m\xi^2\right)}{\left[C^0_{1212}+\left(C^0_{2323}-C^0_{1212}\right)\xi^2\right]} d\xi \tag{3.29}$$

where γ_1^2 and γ_2^2 are the roots of

$$C^0_{3333}C^0_{2323}x^2 - \left(C^0_{1111}C^0_{3333} - 2C^0_{1133}C^0_{2323} - C^0_{1133}{}^2\right)x + C^0_{1111}C^0_{2323} = 0 \tag{3.30}$$

The Eshelby's tensor then can be calculated from the following equation

$$\boldsymbol{S} = \boldsymbol{P} \bullet \boldsymbol{C}_0 \tag{3.31}$$

3.9 Appendix III: Effective Stiffness of Composites with Oriented Particles

Let us start by considering a two-phase composite consisting of a linearly elastic isotropic matrix (phase 0, with the stiffness $\boldsymbol{C}_0$) and linearly elastic spheroidal particles (phase 1, with the stiffness $\boldsymbol{C}_1$). The particles are randomly located in the matrix. The aspect ratio of the spheroidal particles is defined as $\alpha = a_1 / a$ where a_1 and a are the semi-axes of the spheroids [**Figure 3-11 (a)**]. It is assumed that the two phases are perfectly bonded at the interfaces.

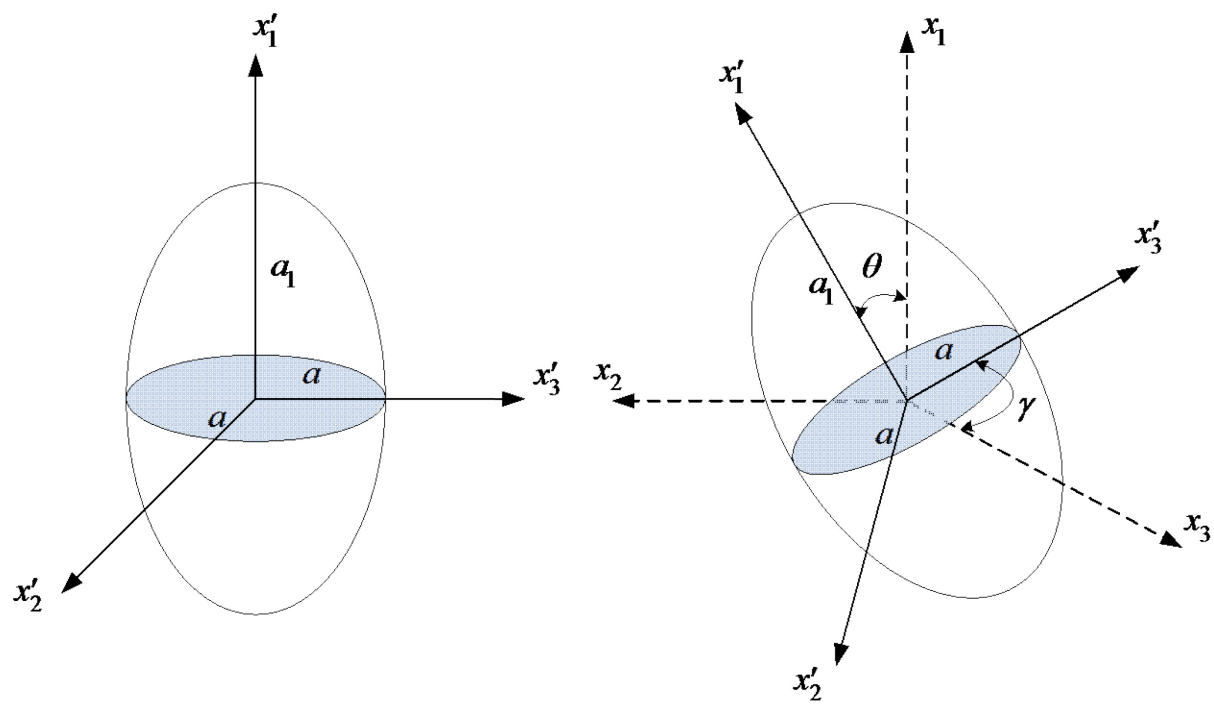

Figure 3-11. (a) The sketch of a spheroid, and (b) transformation between local coordinate system x_i' and global coordinate system x_j

The transformation between local coordinates of particles and global coordinates of composites is demonstrated first. As shown in **Figure 3-11 (b)**, the local axes of a spheroidal inclusion are denoted by the primed coordinate system (x_1', x_2', x_3') with axis x_1' being the symmetric axis of a spheroid. The global axes are represented by the unprimed coordinate system (x_1, x_2, x_3). Each component of the coordinate transformation matrix $[Q_{ij}]$ is simply the cosine between the *i*th primed and *j*th unprimed axes. Thus, we have

$$\{x_i'\} = [Q_{ij}]\{x_j\} \tag{3.32}$$

where the transformation matrix has the following form

$$[Q_{ij}] = \begin{bmatrix} \cos\theta & \sin\theta\cos\gamma & \sin\theta\sin\gamma \\ -\sin\theta & \cos\theta\cos\gamma & \cos\theta\sin\gamma \\ 0 & -\sin\gamma & \cos\gamma \end{bmatrix} \tag{3.33}$$

with θ ($-\pi/2 \le \theta \le \pi/2$) denoting the angle between x_1 and x_1' and γ ($0 \le \gamma \le \pi$) representing the angle between x_3 and x_3'. Therefore, any second-rank tensor, e.g., the stress tensor, can be transformed between the global and the local as

$$\sigma_{ij}' = Q_{ik}Q_{jl}\sigma_{kl} \tag{3.34}$$

or

$$\sigma_{ij} = Q_{ki}Q_{lj}\sigma_{kl}' \tag{3.35}$$

To obtain effective constitutive equations of random heterogeneous composites, one typically performs the ensemble-volume and orientational averaging procedures (homogenizations) within a mesoscopic representative volume element (RVE). In

particular, Ju and Chen [15] performed the ensemble-volume homogenization and derived the governing stress-strain equations for particle-reinforced composites under the applied far-field stress σ^0. In the case of the first-order approximation, the three governing constitutive equations take the form:

$$\begin{aligned} \bar{\sigma} &= \boldsymbol{C}_0 : (\bar{\varepsilon} - \phi\bar{\varepsilon}^*) \\ \bar{\varepsilon} &= \varepsilon^0 + \phi\boldsymbol{S} : \bar{\varepsilon}^* \\ \bar{\varepsilon}^* &= -(\boldsymbol{S} + \boldsymbol{A})^{-1} : \varepsilon^0 \end{aligned} \tag{3.36}$$

where $\bar{\sigma}$, $\bar{\varepsilon}$, and $\bar{\varepsilon}^*$ are the ensemble-volume averaged stress, strain, and eigenstrain tensors of composites, respectively. The corresponding far-field strain is $\varepsilon^0 = \boldsymbol{C}_0^{-1} : \sigma^0$ and the elastic mismatch tensor reads $\boldsymbol{A} = \left(\boldsymbol{C}_1 - \boldsymbol{C}_0\right)^{-1} \bullet \boldsymbol{C}_0$. The effective stiffness tensor of aligned particle-reinforced composites can be easily obtained from the foregoing three governing equations.

When all of the reinforcements of composites are randomly located and randomly oriented in the three-dimensional (3D) space, the orientation-averaging process is further applied to Eq. (3.36). For example, the orientational average of $\bar{\sigma}$ is defined as

$$\langle \bar{\sigma} \rangle \triangleq \int_0^{2\pi} \int_0^{\pi/2} \bar{\sigma} P(\theta, \gamma) \sin\theta d\theta d\gamma \tag{3.37}$$

where the range of two angle θ and γ are $0 \le \theta \le \pi/2$ and $0 \le \gamma \le 2\pi$, respectively. Further, the function $P(\theta, \gamma)$ represents the probability density function of the orientation. The three governing equations of composites together with the random orientation of particles can be formulated as

$$
\begin{aligned}
&\langle \bar{\sigma} \rangle = \boldsymbol{C}_0 : \left(\langle \bar{\varepsilon} \rangle - \phi \langle \bar{\varepsilon}^* \rangle \right) \\
&\langle \bar{\varepsilon} \rangle = \boldsymbol{\Lambda} : \bar{\varepsilon}^* \\
&\langle \bar{\varepsilon}^* \rangle = -\boldsymbol{\Omega} : \varepsilon^0
\end{aligned}
\tag{3.38}
$$

where the fourth-rank tensor $\boldsymbol{\Lambda}$ and $\boldsymbol{\Omega}$ read

$$
\Lambda_{ijkl} = I_{ijkl} - \phi \int_0^{2\pi} \int_0^{\pi/2} Q_{mi} Q_{nj} S_{mnpq} \left(S_{pqst} + A_{pqst} \right)^{-1} Q_{sk} Q_{tl} P(\theta, \gamma) \sin\theta d\theta d\gamma \tag{3.39}
$$

and

$$
\Omega_{ijkl} = \int_0^{2\pi} \int_0^{\pi/2} Q_{mi} Q_{nj} \left(S_{mnpq} + A_{mnpq} \right)^{-1} Q_{pk} Q_{ql} P(\theta, \gamma) \sin\theta d\theta d\gamma \tag{3.40}
$$

It is noted that $\boldsymbol{I}$ signifies the fourth-rank identity tensor. Emanating from Eq. (3.38), the effective elastic stiffness tensor for randomly oriented particle-reinforced composites can be derived as

$$
\langle \bar{\boldsymbol{C}} \rangle = \boldsymbol{C}_0 \bullet \left(\boldsymbol{I} + \phi \boldsymbol{\Omega} \bullet \boldsymbol{\Lambda}^{-1} \right) \tag{3.41}
$$

3.10 Appendix IV: Determination of Tissue-Specific Volume Fractions

The validation of our multi-scale homogenization model requires determination of the volume fraction within the considered representative volume elements.

At the extravascular level, the volume fraction of the osteocyte lacunae, ϕ_{lac}, can be obtained from the polarized light microscopy [32] through

$$\phi_{lac} = \frac{\text{area of lacunae in field of view}}{\text{total area of field of view}} \tag{3.42}$$

The value of 0.025 is selected here based on the confocol images [5], which is consistent with the typical value for any kind of mammalian bone [33].

The volume fraction of apatite crystal, ϕ_{HA}, and collagen, ϕ_{col}, can be determined from weighting experiments of wet, dried and dried demineralized tissues [27, 34, 35] through the following equations.

For wet tissues,

$$\phi_{HA} = WF_{HA} \cdot \frac{\rho_w}{\rho_{HA}} \tag{3.43}$$

$$\phi_{col} = 0.9 \cdot WF_{org} \cdot \frac{\rho_w}{\rho_{col}} \tag{3.44}$$

where WF_{HA} and WF_{org} are the weight fractions of apatite crystal and organic matter of the tissue specimen, ρ_w is the mass density of the wet tissue, $\rho_{HA} = 3.00\ \text{g/cm}^3$ and $\rho_{col} = 1.41\ \text{g/cm}^3$ [27] are the mass densities of apatite crystal and collagen. Eq. (3.44) implies that, in mineralized tissues, about 90% per mass of the organic matter is collagen [27, 36].

For dry tissues,

$$\phi_{HA} = \frac{WF_{HA}}{WF_{HA} + WF_{org}} \cdot \frac{\rho_d}{\rho_{HA}} \tag{3.45}$$

$$\phi_{col} = 0.9 \cdot \frac{WF_{org}}{WF_{HA} + WF_{org}} \cdot \frac{\rho_d}{\rho_{col}} \tag{3.46}$$

where ρ_d is the mass density of the dried tissue.

The volume fraction of the fibrils in the ultrastructure can be determined based on the generalized packing model [27, 30, 37] through the following equations,

$$\phi_{fib} = \phi_{col} \cdot \frac{v_{fib}}{v_{col}}, \qquad v_{fib} = bd_w 5D \tag{3.47}$$

where $v_{col} = 335.6\ \text{nm}^3$ is the volume of a single collagen molecule [27], $b \approx 1.5$ nm is an average length of collagen crosslink for mineralized tissues, $D \approx 67$ nm is the axial period of staggered assemblies of type I collagen, and d_w is the tissue-specific neutron diffraction spacing between collagen molecules depending on the mineralization and the hydration state of the tissue specimen.

The volume fraction of collagen molecule within the fibrils then can be obtained as

$$\phi_{col,fib} = \frac{\phi_{col}}{\phi_{fib}} \tag{3.48}$$

Here we are going to introduce an apatite crystal distribution parameter α_{ef}, which determines the relative amount of apatite crystal in the extrafibrillar space. The volume fraction of apatite crystal in the fibrillar and the extrafibrillar space are then given by

$$\phi_{HA,fib} = \frac{\phi_{HA}\left(1-\alpha_{ef}\right)}{\phi_{fib}} \tag{3.49}$$

$$\phi_{HA,ef} = \frac{\phi_{HA}\alpha_{ef}}{\left(1-\phi_{fib}\right)} \tag{3.50}$$

There are a few publications addressing the value of α_{ef}. Lees et al. [17] reported that 70-75% of the apatite crystal in fully mineralized turkey leg tendon is extrafibrillar and 30-25% is within the fibril. Sasaki et al. [38] estimated that about 77% of the apatite crystal is outside the fibril in bovine femoral cortical bone. Hellmich and Ulm [39] suggested that an average uniform apatite crystal concentration in the non-collagenous space in fully mineralized tissues, which results in

$$\alpha_{ef} = \frac{1-\phi_{fib}}{1-\phi_{col}} \tag{3.51}$$

Finally, from equations (3.42), (3.47) to (3.50), the volume fractions within the considered representative volume elements can be determined.

3.11 References

1. Hellmich, C., J.F. Barthelemy, and L. Dormieux, *Mineral-collagen interactions in elasticity of bone ultrastructure - a continuum micromechanics approach.* European Journal of Mechanics a-Solids, 2004. **23**(5): p. 783-810.
2. Swadener, J.G., J.Y. Rho, and G.M. Pharr, *Effects of anisotropy on elastic moduli measured by nanoindentation in human tibial cortical bone.* Journal of Biomedical Materials Research, 2001. **57**(1): p. 108-112.
3. Lees, S. and F. Rollins, *Anisotropy in hard dental tissues.* J. Biomech., 1972. **5**: p. 557-566.
4. Fratzl, P., et al., *Nucleation and growth of mineral crystals in bone studied by small-angle X-ray scattering.* Calcified Tissue International, 1991. **48**(6): p. 407-413.
5. Ascenzi, M.-G. and A. Lomovtsev, *Collagen orientation patterns in human secondary osteons, quantified in the radial direction by confocal microscopy.* Journal of Structural Biology, 2006. **153**(1): p. 14-30.
6. Landis, W.J., et al., *Mineralization of Collagen May Occur on Fibril Surfaces: Evidence from Conventional and High-Voltage Electron Microscopy and Three-Dimensional Imaging.* Journal of Structural Biology, 1996. **117**(1): p. 24-35.
7. Rho, J.-Y., T.Y. Tsui, and G.M. Pharr, *Elastic properties of human cortical and trabecular lamellar bone measured by nanoindentation.* Biomaterials, 1997. **18**(20): p. 1325-1330.

8. Cuy, J.L., et al., *Nanoindentation mapping of the mechanical properties of human molar tooth enamel.* Archives of Oral Biology, 2002. **47**(4): p. 281-291.

9. Jager, I. and P. Fratzl, *Mineralized Collagen Fibrils: A Mechanical Model with a Staggered Arrangement of Mineral Particles*, 2000. p. 1737-1746.

10. Hengsberger, S., A. Kulik, and P. Zysset, *A combined atomic force microscopy and nanoindentation technique to investigate the elastic properties of bone structural units.* Eur Cell Mater, 2001. **1**: p. 12-7.

11. Petruska, J.A. and A.J. Hodge, *Subunit Model for Tropocollagen Macromolecule.* Proceedings of the National Academy of Sciences of the United States of America, 1964. **51**(5): p. 871-&.

12. Gilmore, R.S. and J.L. Katz, *Elastic properties of apatites.* Journal of Materials Science, 1982. **V17**(4): p. 1131-1141.

13. Rey, C., et al., *The Carbonate Environment in Bone-Mineral: A Resolution-Enhanced Fourier Transform Infrared Spectroscopy Study.* Calcified Tissue International, 1989. **45**(3): p. 157-164.

14. Sasaki, N. and S. Odajima, *Stress-strain curve and young's modulus of a collagen molecule as determined by the X-ray diffraction technique.* Journal of Biomechanics, 1996. **29**(5): p. 655-658.

15. Ju, J.W. and T.M. Chen, *Micromechanics and Effective Moduli of Elastic Composites Containing Randomly Dispersed Ellipsoidal Inhomogeneities.* Acta Mechanica, 1994. **103**(1-4): p. 103-121.

16. Peters, F., K. Schwarz, and M. Epple, *The structure of bone studied with synchrotron X-ray diffraction, X-ray absorption spectroscopy and thermal analysis.* Thermochimica Acta, 2000. **361**(1-2): p. 131-138.

17. Lees, S., et al., *The loci of mineral in turkey leg tendon as seen by atomic force microscope and electron microscopy.* Calcified Tissue International, 1994. **55**(3): p. 180-189.

18. Fratzl, P., S. Schreiber, and K. Klaushofer, *Bone mineralization as studied by small-angle X-ray scattering.* Connective Tissue Research, 1996. **34**(4): p. 247-254.

19. Eppell, S.J., et al., *Shape and size of isolated bone mineralites measured using atomic force microscopy.* Journal of Orthopaedic Research, 2001. **19**(6): p. 1027-1034.

20. Benezra Rosen, V., L.W. Hobbs, and M. Spector, *The ultrastructure of anorganic bovine bone and selected synthetic hyroxyapatites used as bone graft substitute materials.* Biomaterials, 2002. **23**(3): p. 921-928.

21. Ju, J.W. and T.M. Chen, *Effective elastic moduli of two-phase composites containing randomly dispersed spherical inhomogeneities.* Acta Mechanica, 1994. **V103**(1): p. 123-144.

22. Lees, S., J.M. Ahern, and M. Leonard, *Parameters Influencing The Sonic Velocity in Compact Calcified Tissues of Various Species.* Journal of the Acoustical Society of America, 1983. **74**(1): p. 28-33.

23. Sun, L.Z. and J.W. Ju, *Elastoplastic modeling of metal matrix composites containing randomly located and oriented spheroidal particles.* Journal of Applied Mechanics-Transactions of the Asme, 2004. **71**(6): p. 774-785.

24. McCreadie, B.R., et al., *Osteocyte lacuna size and shape in women with and without osteoporotic fracture.* Journal of Biomechanics, 2004. **37**(4): p. 563-572.

25. Wang, X., et al., *Age-related changes in the collagen network and toughness of bone.* Bone, 2002. **31**(1): p. 1-7.

26. Zioupos, P., J.D. Currey, and A.J. Hamer, *The role of collagen in the declining mechanical properties of aging human cortical bone.* Journal of Biomedical Materials Research, 1999. **45**(2): p. 108-116.

27. Lees, S., *Considerations regarding the structure of the mammalian mineralized osteoid from viewpoint of the generalized packing model.* Connect Tissue Res, 1987. **16**(4): p. 281-303.

28. Fratzl, P., N. Fratzlzelman, and K. Klaushofer, *Collagen packing and mineralization. An x-ray scattering investigation of turkey leg tendon.* Biophysical Journal, 1993. **64**(1): p. 260-266.

29. Pineri, M.H., M. Escoubes, and G. Roche, *Water-collagen interactions: Calorimetric and mechanical experiments.* Biopolymers, 1978. **17**(12): p. 2799-2815.

30. Lees, S., M. Pineri, and M. Escoubes, *A generalized packing model for type I collagen.* International Journal of Biological Macromolecules, 1984. **6**(3): p. 133-136.

31. Laws, N., *A note on penny-shaped cracks in transversely isotropic materials.* Mechanics of Materials, 1985. **4**(2): p. 209-212.

32. Ascenzi, M.-G., J. Gill, and A. Lomovtsev, *Orientation of collagen at the osteocyte lacunae in human secondary osteons.* Journal of Biomechanics, 2008. **41**(16): p. 3426-3435.

33. Cowin, S.C., *Bone poroelasticity.* Journal of Biomechanics, 1999. **32**(3): p. 217-238.

34. Lees, S., J.D. Heeley, and P.F. Cleary, *Study of Some Properties of a Sample of Bovine Cortical Bone Using Ultrasound.* Calcified Tissue International, 1979. **29**(2): p. 107-117.

35. Lees, S., et al., *Comparison of Dosage-Dependent Effects of Beta-Aminopropionitrile, Sodium-Fluoride, and Hydrocortisone on Selected Physical-Properties of Cortical Bone.* Journal of Bone and Mineral Research, 1994. **9**(9): p. 1377-1389.

36. Weiner, S. and H.D. Wagner, *The material bone: Structure mechanical function relations.* Annual Review of Materials Science, 1998. **28**: p. 271-298.

37. Fritsch, A. and C. Hellmich, *`Universal' microstructural patterns in cortical and trabecular, extracellular and extravascular bone materials: Micromechanics-based prediction of anisotropic elasticity.* Journal of Theoretical Biology, 2007. **244**(4): p. 597-620.

38. Sasaki, N., et al., *Atomic force microscopic studies on the structure of bovine femoral cortical bone at the collagen fibril-mineral level.* Journal of Materials Science-Materials in Medicine, 2002. **13**(3): p. 333-337.

39. Hellmich, C. and F.J. Ulm, *Average hydroxyapatite concentration is uniform in the extracollagenous ultrastructure of mineralized tissues: evidence at the 1–10-μm scale.* Biomechanics and Modeling in Mechanobiology, 2003. **2**(1): p. 21-36.